Title: **Computations of Flow Noise
in Two Dimensions**

Author(s): Karen Pao
Christopher R. Anderson

Submitted to:

http://lib-www.lanl.gov/la-pubs/00412928.pdf

Los Alamos
NATIONAL LABORATORY

Computations of Flow Noise in Two Dimensions

Karen Pao *
Computing, Information, and Communications Division
Los Alamos National Laboratory
Los Alamos, NM 87545

Christopher R. Anderson
Department of Mathematics
University of California
Los Angeles, CA 90024

Send proofs to :
Karen Pao
CIC-3, MS B256
Los Alamos National Laboratory
Los Alamos, NM 87545

Suggested running head: *Computations of Flow Noise*

Abstract

We develop a numerical method for computing the sound generated by unsteady low speed flows in two space dimensions. Direct solutions of the aerodynamic sound generation problem can pose computational difficulties because the acoustics and the fluid flow vary on different time and length scales. Our approach is to compute the acoustic waves separately from the fluid motion. The procedure is based on an asymptotic decomposition by Klainermann and Majda, who represent aerodynamic sound as a correction to the incompressible component of a fluid flow. The acoustic correction satisfies a system of partial differential equations; our work focuses on the numerical solution of these acoustical equations, and a numerical technique for coupling the acoustics and the incompressible flow. The sounds generated by various configurations of vortices are computed.

1   Introduction

One of the primary problems in the computation of acoustic signals induced
by low Mach number fluid motion is the presence of phenomena occuring on
different scales. In low Mach number flows, the fluid flow velocity is much
less than the speed of sound. In addition, the scale of the vortical structures
which produce sound are often much smaller than the acoustic wavelength.
Thus, one must choose time and spatial discretizations that will simultaneously
resolve the fast-traveling sound waves and the fine scale vortex motions. Such
restrictions may render direct numerical solution of the slightly compressible
problem infeasible. To overcome the difficulties caused by these disparities in
scales, we may compute the fluid motion using the incompressible equations and
then recover the acoustics by an auxiliary computation. This is the basic idea
behind approaches to aeroacoustics suggested by Lighthill [1], Powell [2], and
many others ([3]–[8]).

In our work we have undertaken to develop an approach to computing acous-
tic signals in the flows, by separating the fluid flow into the incompressible com-
ponent and the acoustics. The theoretical foundation for this work is provided
by an asymptotic expansion due to Klainermann and Majda [10] [11]. In their
decomposition, the slightly compressible flow field is represented as an incom-
pressible flow plus an acoustical correction. Klainermann and Majda have shown
that the acoustical correction satisfies a system of linear hyperbolic equations
whose coefficients are functions of the incompressible flow variables.

In section 2, we summarize the derivation of the equations of acoustics. Our
numerical method is presented in sections 3 and 4. Computational results are
presented in section 5.

2   Formulation

We briefly outline the derivation of the acoustics equations described in Klainer-
mann and Majda [11]. Consider the equations of isentropic inviscid compressible
flows

$$\rho_t + v \cdot \nabla \rho + \rho \nabla \cdot v = 0, \tag{1}$$

$$\rho(v_t + v \cdot \nabla v) + \nabla p = 0, \tag{2}$$

with initial conditions

$$\rho(x, 0) = \rho_0(x), v(x, 0) = v_0(x).$$

Here v is the compressible velocities, ρ is the fluid density, and p is the pressure.
The pressure and the density are related by the equation of state

$$p = p(\rho).$$

4

Here we shall assume that the fluid is an ideal gas, that is,

$$p = \rho^{\gamma},$$

where γ is the ratio of the specific heats.

We shall non-dimensionalize these equations by a change of variables: scale the variables by $\rho_m = \max_x \rho_0(x)$, $|v_m| = \max_x |v_0(x)|$, and let

$$\tilde{v} = \frac{v}{|v_m|}, \tag{3}$$

$$\tilde{\rho} = \frac{\rho}{\rho_m}, \tag{4}$$

$$t' = |v_m| t. \tag{5}$$

Dropping the tilde's and reverting to the unprimed independent variables, we have

$$p_t + v \cdot \nabla p + \gamma p(\rho) \nabla \cdot v = 0 \tag{6}$$

$$\rho(v_t + v \cdot \nabla v) + \frac{1}{M^2} \nabla p = 0 \tag{7}$$

with the initial conditions

$$p(x, 0) = p_0(x), v(x, 0) = v_0(x).$$

Here M is the Mach number, defined as

$$M = \frac{\gamma^{1/2} |v_m|}{(dp/d\rho)|_{\rho_m}^{1/2}}. \tag{8}$$

It is essentially the ratio of the flow speed and the sound speed.

The equations of inviscid, incompressible flow are

$$\rho_0(v_t^{\infty} + v^{\infty} \cdot \nabla v^{\infty}) + \nabla p^{\infty} = 0, \tag{9}$$

$$\nabla \cdot v^{\infty} = 0, \tag{10}$$

with initial conditions

$$p^{\infty}(x, 0) = p_0^{\infty}(x), v^{\infty}(x, 0) = v_0^{\infty}(x).$$

Here p^{∞}, v^{∞} are the incompressible velocities and pressure, respectively, and ρ_0 is the density, which is a constant. It has been shown (for example, in [10]) that, in the singular limit as M goes to zero in (6), (7), we obtain (9), (10). We are interested in the case $M \ll 1$.

Klainermann and Majda [10] [11] have shown that the total pressure and velocity may be expanded about the incompressible velocity v^{∞} and the constant equilibrium pressure P_0:

$$p = P_0 + M^2(p^{\infty} + p_1) + O(M^3), \tag{11}$$

$$v = v^{\infty} + M v_1 + O(M^2), \tag{12}$$

where (p_1, v_1) satisfy

$$\rho_0(v_{1t} + v^\infty \cdot \nabla v_1 + v_1 \cdot \nabla v^\infty) + \frac{1}{M}\nabla p_1 = 0, \tag{13}$$

$$p_{1t} + v^\infty \cdot \nabla p_1 + \gamma P_0 \frac{1}{M}\nabla \cdot v_1 = -(p_t^\infty + v^\infty \cdot \nabla p^\infty), \tag{14}$$

with initial conditions

$$\begin{aligned}
p_1(x, 0) &= p_1^0(x) - p^\infty(x, 0), \\
v_1(x, 0) &= v_1^0(x).
\end{aligned}$$

In general, (p_1, v_1) may contain very fast acoustical oscillations.

In flows where the above asymptotic expansions above are valid, the pressure variations should be much less than the velocity variations for all time. In particular, the initial conditions for the compressible Euler's equations must satisfy

$$\begin{aligned}
p(x, 0) &= P_0 + O(M^2), \\
v(x, 0) &= v_0^\infty(x) + O(M), \\
\nabla \cdot v_0^\infty(x) &= 0
\end{aligned}$$

in order for $v \to v^\infty$ uniformly as $M \to 0$.

Note that when the incompressible flow is identically zero, equations (13) (14) are reduced to the classical wave equations

$$\begin{aligned}
v_{1t} + \frac{1}{M}\nabla p_1 &= 0, \\
p_{1t} + \frac{1}{M}\nabla \cdot v_1 &= 0,
\end{aligned}$$

with the appropriate initial conditions.

The asymptotic approach described above is not very different from those commonly used in the aeroacoustics community. Typically, one would start from the classical wave equation with a source term, derived from the equations of compressible flows by Lighthill [1]:

$$\frac{\partial^2}{\partial t^2}\rho - c^2\nabla^2\rho = \frac{\partial^2}{\partial x_i \partial x_j}\rho v_i v_j.$$

Various approximations of the source term can be made, then an "exact" solution may be found, usually in the far field, by using Green's functions. For example, in isentropic flow, one commonly used solution is due to Powell [2] :

$$p(\mathrm{x}, t) = \int G(\mathrm{x}, \mathrm{x}', t, t')Q(\mathrm{x}', t')d^3x'dt',$$

6

where
$$Q = -\rho_0 \nabla \cdot (\omega \times v^\infty) - (\frac{1}{c^2}\frac{\partial^2}{\partial t^2} - \nabla^2)(\frac{\rho_0 |v^\infty|^2}{2}),$$

and ω is the vorticity. Using singular perturbation techniques, Crow [4] has shown that, to the highest order, the source of aerodynamic sound can be written in terms of the incompressible part of the flow. The equations (13) (14) can in fact be written as a wave equation for p_1, with a source term that approximates Lighthill's source term above to $O(M^2)$. This could be seen by substituting the asymptotic expansions (11) and (12) into Lighthill's wave equation (properly nondimensioned), and comparing the result with the corresponding source term in (13) (14) (see [12] for detail).

3 Algorithm Design

To solve the equations of slightly compressible flow directly using an explicit finite difference method, one must choose time steps according to the Courant-Friedrichs-Lewy (CFL) condition, Essentially, this condition implies that for numerical stability waves cannot travel more than one grid cell per time step. When compressible flow velocities are much less than the sound speed, the fastest moving waves are the acoustic waves. In such cases one must use a time step on the order of the ratio of the spatial discretization to the sound speed. With regard to resolving the fluid motion, this time step would be excessively small, and would make simulations of low speed compressible flow computationally expensive.

In Klainermann and Majda's asymptotic expansions, the fast-moving part of the slightly compressible flow, or the acoustics, has been separated from the slow-moving part, or the incompressible flow. By separating the acoustics from the flow, we may compute the incompressible flow using a time step determined by the flow speed only, and the acoustics using a time step determined by the sound speed. It may seem that we have not gained anything, since the acoustics computations may still require a small time step. However, an assumption in the derivation of these equations is that with proper initial conditions, the wavelengths of the acoustic waves represented by the asymptotics must be large compared to the size of the acoustic source. To see that, substitute the asymptotic expansions (11) and (12) into (7). in order to balance the $O(1)$ terms we must have
$$\nabla p_1 \sim O(M).$$

This implies that the sound pressure cannot change much over a short distance. Thus, only coarse spatial resolution may be required for the acoustic waves, and by the same CFL condition, large time steps can actually be taken for the acoustics computations as well.

With the above scaling arguments in mind, we design the scheme described below. We use one grid to resolve the incompressible flow and another grid
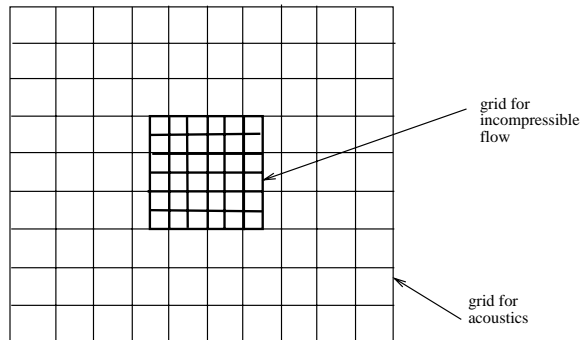
Figure 1: The layout of the grids used in the computations.

to resolve the acoustics. The grid for the incompressible flow will be a small, fine grid, near the center of the computational domain. Since the production of sound by a fluid is related to the dynamics of vorticity, the grid should at least contain any non-zero vorticity in the flow (As we will see in our computational experiments, the grid actually needs to be larger than that). A larger, coarse grid, which extends beyond the incompressible flow grid, is used for the acoustics. On this grid the linear system of equations (13) and (14) are solved using a finite difference method. The incompressible flow field on the large grid outside the small domain is assumed to be constant or potential (zero vorticity). Figure 1 shows the typical layout of the grids.

The two computations "communicate" through the source term in (14). The source term, the convective derivative of the incompressible pressure, is resolved on a fine grid, while the acoustics is to be computed on a coarse grid. Thus we need to capture the essential sound producing features on the coarse grid. One may devise various ways to represent the source on the coarse acoustic grid. The easiest is to use the fine grid values on the coarse grid where the coarse grid meets the fine grid. Alternately, one may average the source over all small cells contained in a given large cell on the coarse grid. For the numerical experiments presented in this paper, we have chosen the first technique. Other techniques are under investigation.

The two problems could be advanced in tandem with the same time steps. If one wishes, one can take smaller time steps in the acoustics computations; if the incompressible flow data are available in time intervals such that the flow is resolved, then any incompressible information necessary for the acoustics computations may be obtained by performing interpolations in time. Since the source of sound is derived from the incompressible flow, however, one must take care not to advance the acoustics before the incompressible variables have been obtained at any given time. Figure 2 shows a typical time-marching scheme.
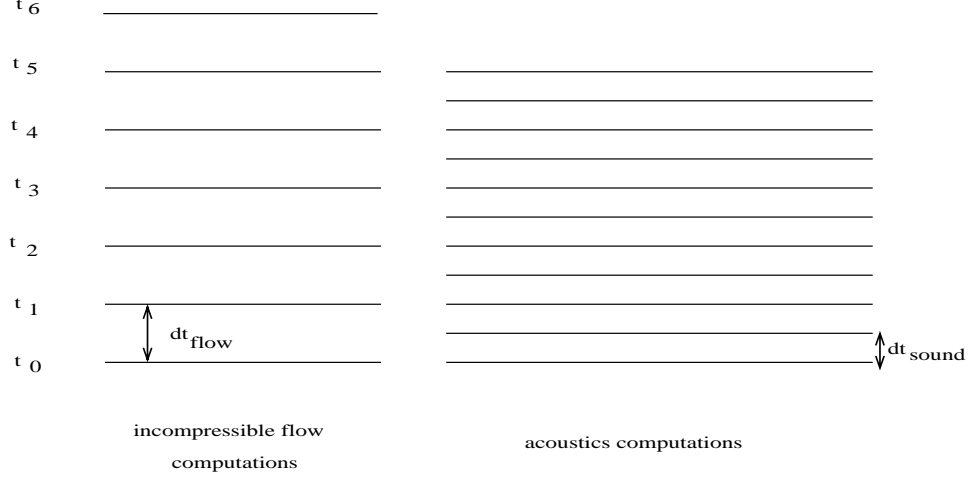
Our algorithm is as follows:

Figure 2: The different time steps for the flow computations and the acoustics computations. Here $n_{acoustics} = 2$. If a second order interpolation is used, for example, then t_n, t_{n+1} would be computed before the acoustics is advanced from t_n.

For $n = 1$: n_{final}

- Advance the incompressible flow variables v^{∞} on the fine grid to the next time level

- Find $v_t^{\infty,n}$ by a difference approximation

- Recover $p^{\infty,n}$, $p_t^{\infty,n}$ from $v^{\infty,n}$, $v_t^{\infty,n}$ on the fine grid

- Compute $f^n = -(p_t^{\infty,n} + v^{\infty,n} \cdot \nabla p^{\infty,n})$ on the fine grid

- Put the source term and the flow variables at t^n on the coarse grid

- Advance acoustics from t_n to t_{n+1} in $n_{acoustics}$ steps; interpolate the flow variables in time to obtain the coefficients and the source term in each substep.

end

4   Numerical Implementation

Our procedure for determining the acoustic signals assumes that one has available the results of an incompressible flow calculation. In general, the incom-

pressible flow solution can be generated by any numerical method. In our computations the incompressible flow field was provided by a discrete vortex method [15]. This method was chosen because it provides approximate solutions to two dimensional, inviscid, incompressible flow, with rather minimal computational effort. The method also provides solutions with the qualitative features of high Reynold's number flows—that is, time-dependent flows which consist of interacting concentrated vortex structures. Thus, the vortex method was particularly useful as a tool in our investigations of the appropriate computational strategy for determining the acoustic signal.

While the vortex method is Lagrangian, and the computational variable is the vorticity $\omega = \nabla \times v^\infty$, it is possible to extract from the solutions the values of the flow velocities v^∞ on the fine, inner grid. It is convenient to have the flow velocities on a grid, because we need to compute the incompressible pressure p^∞. The pressure can be recovered by solving the Poisson's equation

$$\nabla^2 p^\infty \quad = \quad -\rho_0 \text{ div } (v^\infty \cdot \nabla) v^\infty, \tag{15}$$

with the Neumann boundary conditions

$$\frac{\partial p^\infty}{\partial n} \quad = \quad -\rho_0 \mathrm{n} \cdot (v_t^\infty + v^\infty \cdot \nabla v^\infty) \tag{16}$$

evaluated at the boundaries of the small, inner grid. We in fact solve for p_t^∞, the time derivative of the pressure, since that is required in the source term. p_t^∞ satisfies a similar Poisson's equation, which may be obtained by taking the time derivative of (15), with the boundary condition obtained by taking the time derivative of (16). The term $v^\infty \cdot \nabla p^\infty$ may be computed without solving for p^∞, since by equation (9),

$$v^\infty \cdot \nabla p^\infty = -v^\infty \cdot \rho_0 (v_t^\infty + v^\infty \cdot \nabla v^\infty),$$

and all terms on the right hand side would be computed in the course of solving for p_t^∞.

The system (13) and (14) can be solved with any numerical method for hyperbolic systems. We have implemented a fourth-order Runge-Kutta time stepping and a fourth-order centered differencing in space with artificial viscosity, with first-order absorbing boundary conditions described in [13] to represent an infinite domain by a finite one. We have also implemented a robust upwind scheme described in [14].

5   Numerical Experiments

Here we present the numerical results for sound generated by a finite vortex sheet and by a collection of vortices that simulate a wake.
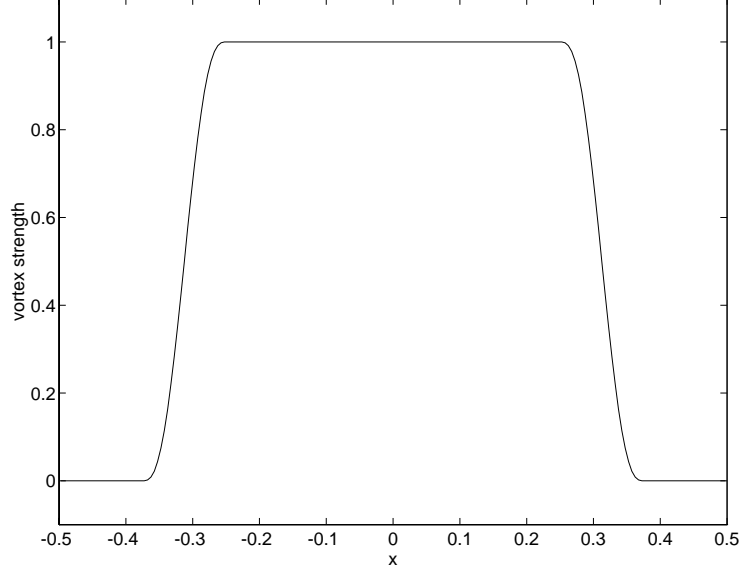
10

Figure 3: The strength of the finite vortex sheet as a function of initial length.

5.1 Sound Generation by a Finite Vortex Sheet

We compute the sound generated by a finite vortex sheet. This vortex sheet has constant strength in the middle, and the strength falls off rapidly but smoothly to 0 at the two ends. Figure 3 shows the strength function in the vortex sheet. This sheet of vorticity is represented by placing N vortex blobs of radius δ of strength

$$\frac{1}{N} \cdot \begin{cases} 0, & |x| > \frac{3}{8} \\ 1, & |x| < \frac{1}{4} \\ 10(8x+3)^3 - 15(8x+3)^4 + 6(8x+3)^5, & -\frac{3}{8} \le x \le -\frac{1}{4} \\ 10(3-8x)^3 - 15(3-8x)^4 + 6(3-8x)^5, & \frac{1}{4} \le x \le \frac{3}{8} \end{cases}$$

on the interval $[-1/2, 1/2]$ along the x-axis. The distribution of vorticity has been chosen so that the vortex sheet strength vanishes at the tips of the sheet and is three times continuously differentiable.

As the vortex sheet evolves, the ends of the vortex sheet roll up into two concentrated vortices. These two vortices then precess in a counterclockwise direction. Figure 4 shows the evolution of such a vortex sheet in time. A typical acoustic pressure contour plot for such computations is shown in figure 5. Sound waves "spiral out" from the source region as the vortex sheet rolls up.

First we study our method by computing the acoustics field due to the finite vortex sheet characterized by $N = 200$, $\delta = 0.25$, with parameters chosen to
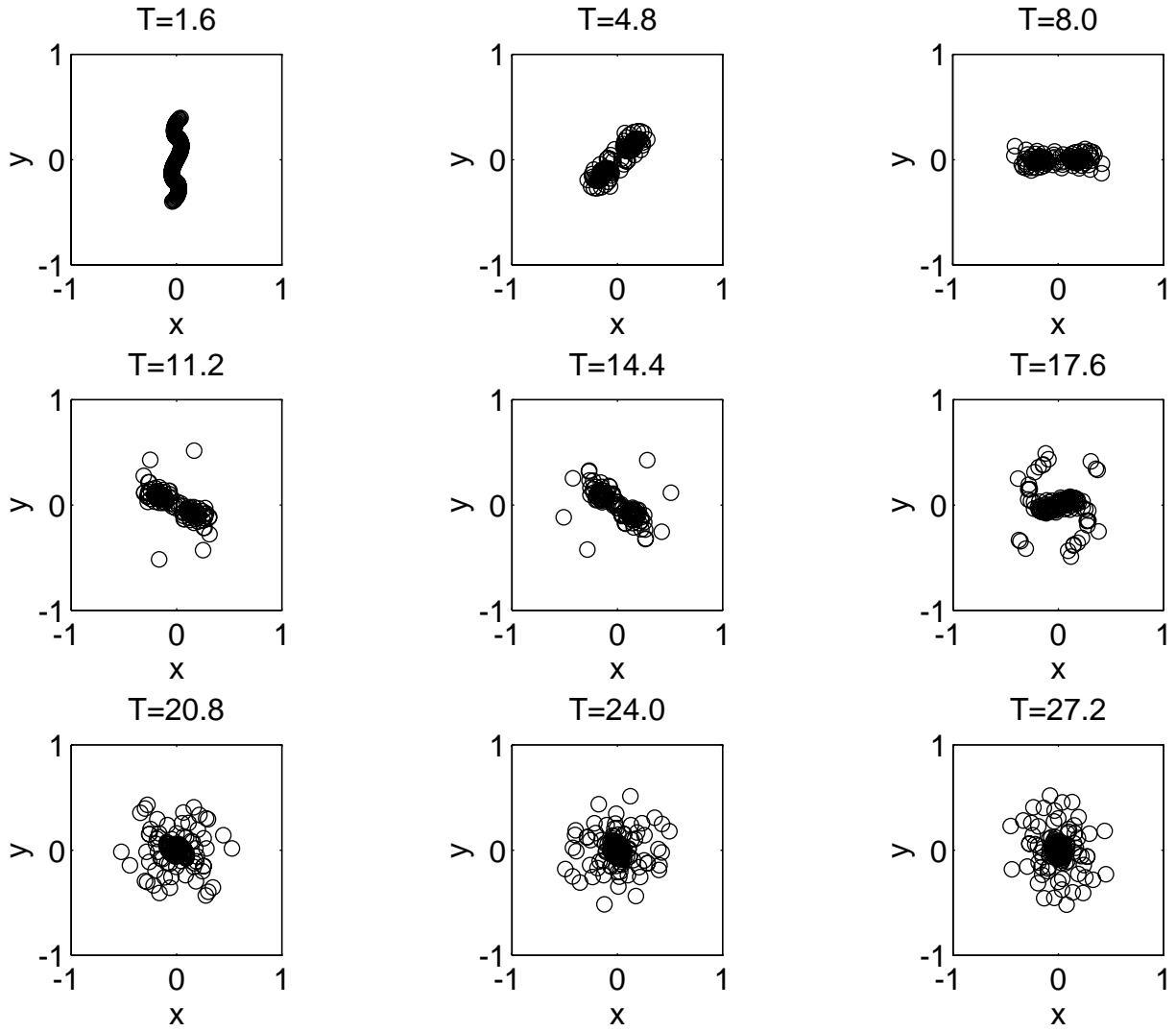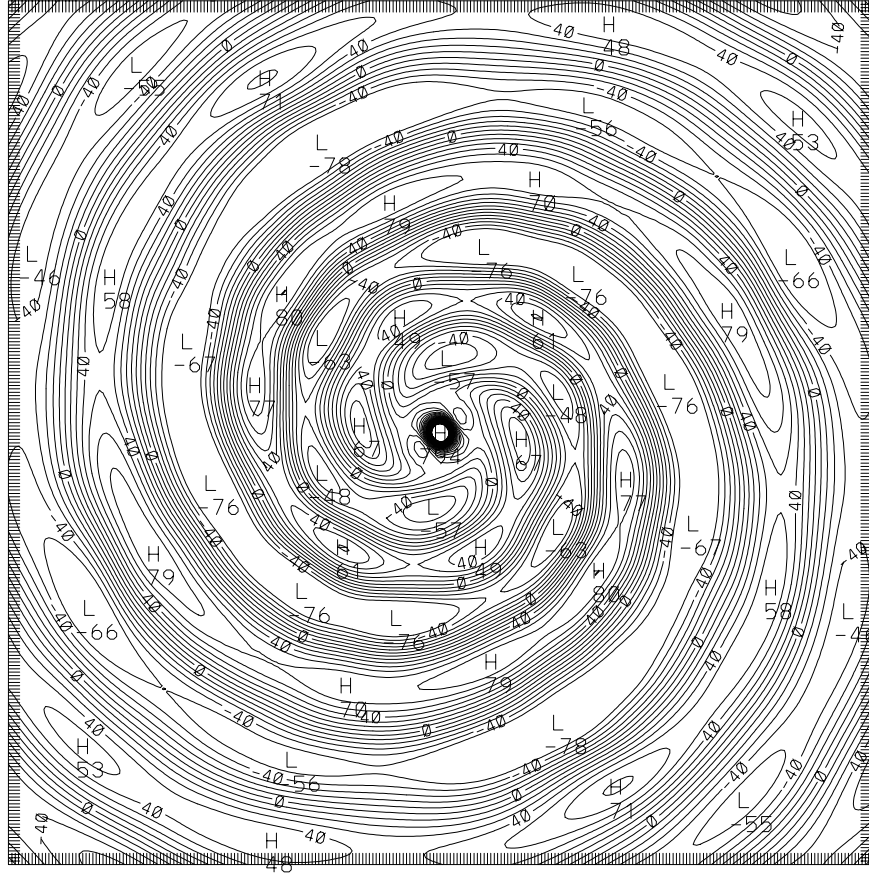
11

Figure 4: The positions of the vortex blobs in a finite vortex sheet at various times T. Here $N = 200$, blob radius is $\delta = 0.25$.

CONTOUR FROM -0.50000E-02 TO 0.34000E-01 CONTOUR INTERVAL OF 0.10000E-02 PT(3,3)= -0.14334E-02 LABELS SCALED BY 10000.

Figure 5: The acoustic pressure contours on $[-8, 8] \times [-8, 8]$ at $T = 20$. Here $N = 200$, blob radius is $\delta = 0.25$.
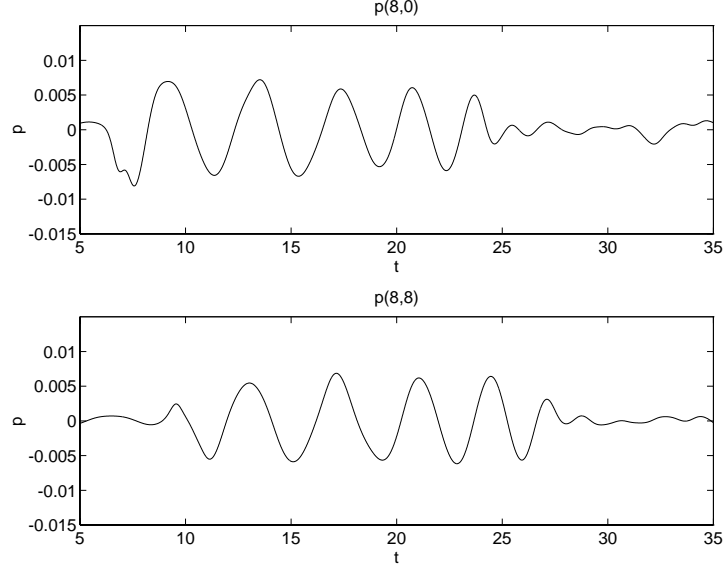
Figure 6: The acoustic pressure near $(8,0)$ (top) and $(8,8)$ (bottom) in time. The acoustics computations are performed on the region $[-8,8] \times [-8,8]$ with $\triangle x = \triangle y = 1/64$. The flow is computed on the same region with the same resolution.

correspond to a Mach number of about 0.35, for various spatial resolutions and flow computation regions. We have arbitrarily chosen two points, one near $(8,0)$, the other near $(8,8)$, to measure the acoustic pressure in time, instead of examining the entire pressure field at various times.

We need to know how to choose a region on which the incompressible flow and the acoustic source are computed. We shall make this choice empirically by studying the acoustics field on a variety of flow regions and resolutions. In these experiments, we compute the acoustics field on the region $[-8,8] \times [-8,8]$, with meshes of 128×128 and 256×256 panels. We let the flow computation region be $[-2,2] \times [-2,2], [-4,4] \times [-4,4], [-6,6] \times [-6,6]$, and $[-8,8] \times [-8,8]$, with resolutions of $\triangle x = \triangle y = 1/8, 1/16, 1/32$. Runs where the resolution of the acoustics computations is finer than that of the flow computations are omitted. A time step of $\triangle t = 0.02$ is used in both the flow computations and the acoustics computations. The solutions are advanced up to time $t = 50$. As an "exact" solution, we compute the acoustics on the region $[-8,8] \times [-8,8]$ with $\triangle x = \triangle y = 1/64$, the flow on the same region with the same resolution, and both with $\triangle t = 0.01$. This exact solution at $(8,0)$ and $(8,8)$ is plotted in figure 6.

For the same resolutions in the acoustics and the incompressible computa-
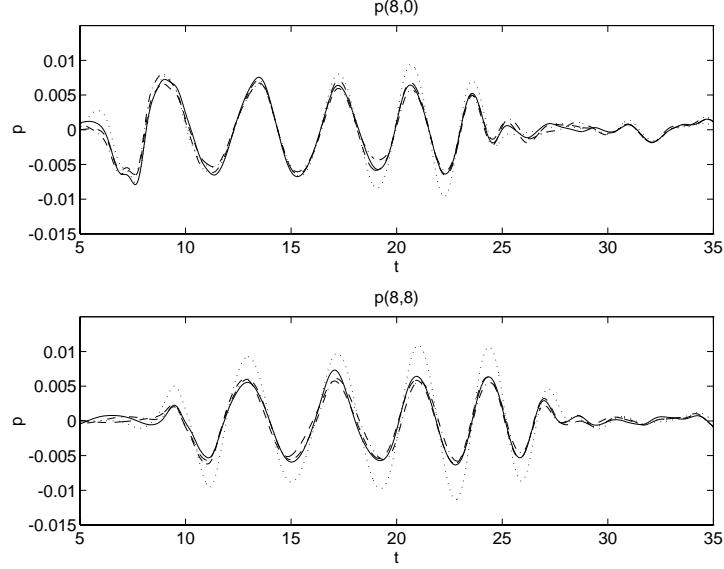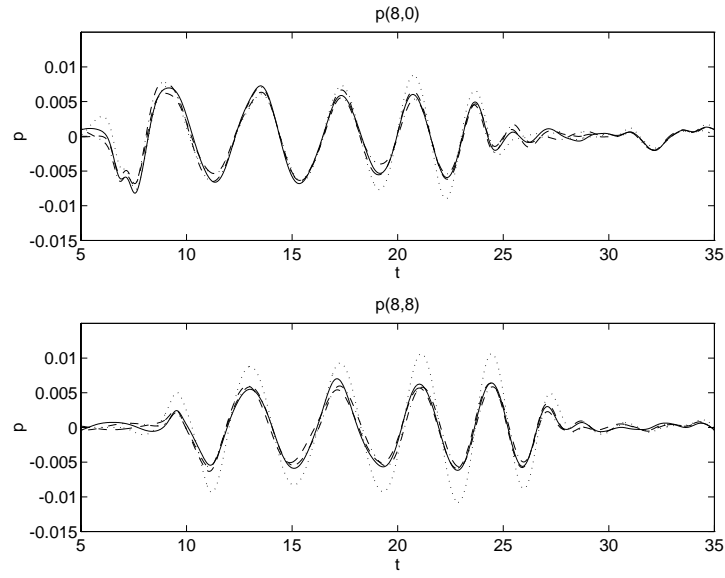
14

Figure 7: The acoustic pressure near $(8,0)$ (top) and $(8,8)$ (bottom) in time. The acoustics computations are performed on the region $[-8,8] \times [-8,8]$ with 128×128 panels, and the flow is computed with the resolution of $\triangle x = \triangle y = 1/16$, on the regions $[-2,2] \times [-2,2]$ (dotted), $[-4,4] \times [-4,4]$ (dash-dot), $[-6,6] \times [-6,6]$ (dashed), and $[-8,8] \times [-8,8]$ (solid).

tions, we compare the acoustic signals computed using different source regions. Figure 7 shows the acoustic signals in time near $(8,0)$ and $(8,8)$ computed using the acoustics region of $[-8,8] \times [-8,8]$ with 128×128 panels, and the flow regions of $[-2,2] \times [-2,2]$,$[-4,4] \times [-4,4]$,$[-6,6] \times [-6,6]$, and $[-8,8] \times [-8,8]$, with $64 \times 64, 128 \times 128, 192 \times 192, 256 \times 256$ panels, respectively. Figure 8 shows the acoustic signals in time near $(8,0)$ and $(8,8)$ computed using the acoustics region of $[-8,8] \times [-8,8]$ with 256×256 panels, with the same flow regions and resolutions. We see that, although the vorticity has compact support contained in $[-1,1] \times [-1,1]$, the incompressible flow region $[-2,2] \times [-2,2]$ is not sufficiently large to contain the acoustic source. The sources computed in the other three regions are similar enough, that the acoustic signals are comparable.

For another comparison of our data, we compute discrete analogue the root-mean-square (rms) values of the acoustic signals over the time interval of length T, where the acoustic signals exhibit periodic behavior. The rms value of the acoustic signal at a point X is defined as

$$p_{rms} = (\frac{1}{T} \int_T p(X,t)^2 dt)^{1/2},$$

15

Figure 8: The acoustic pressure near $(8,0)$ (top) and $(8,8)$ (bottom) in time. The acoustics computations are performed on the region $[-8,8] \times [-8,8]$ with 256×256 panels, and the flow is computed with the resolution of $\triangle x = \triangle y = 1/16$, on the regions $[-2,2] \times [-2,2]$ (dotted), $[-4,4] \times [-4,4]$ (dash-dot), $[-6,6] \times [-6,6]$ (dashed), and $[-8,8] \times [-8,8]$ (solid).

	[−4, 4] × [−4, 4]			[−6, 6] × [−6, 6]			[−8, 8] × [−8, 8]	
	1/8	1/16	1/32	1/8	1/16	1/32	1/8	1/16
128 × 128	4.462	4.502	4.497	4.498	4.553	4.549	4.659	4.712
256 × 256	N/A	4.411	4.411	N/A	4.364	4.365	N/A	4.548

Table I: The root-mean-square values $\times 10^{-3}$ of the acoustic signals near $(8, 0)$ over the time interval $[8, 23]$. The acoustic pressure is computed on the region $[−8, 8] \times [−8, 8]$ with $\triangle x = \triangle y = 1/8$ (128×128 panels) and $1/16$ (256×256 panels). The flow is computed on the regions $[−4, 4] \times [−4, 4]$, $[−6, 6] \times [−6, 6]$,$[8, 8] \times [−8, 8]$, with resolutions of $\triangle x = \triangle y = 1/8, 1/16, 1/32$. Computations where the acoustics field would have finer resolution than the flow field are omitted. The "exact" solution has an rms value of 4.526×10^{-3} over the time interval $[8, 23]$.

	[−4, 4] × [−4, 4]			[−6, 6] × [−6, 6]			[−8, 8] × [−8, 8]	
	1/8	1/16	1/32	1/8	1/16	1/32	1/8	1/16
128 × 128	3.899	4.077	4.086	3.937	4.116	4.125	4.147	4.324
256 × 256	N/A	4.048	4.055	N/A	4.020	4.028	N/A	4.248

Table II: The rms values $\times 10^{-3}$ of the acoustic signals near $(8, 8)$ over the time interval $[10, 25]$. The "exact" solution has an rms value of 4.223×10^{-3}.

and its discrete analogue is

$$p_{discrete\ rms} = (\frac{\triangle t}{T} \sum_i p(X, t_i)^2)^{1/2},$$

where t_i is within the specified time interval. In this test problem, the time interval corresponds to where the signals are the strongest. For the point $(8, 0)$, the time interval is approximately $[8, 23]$; for $(8, 8)$, approximately $[10, 25]$. These intervals are chosen by looking at the plots of acoustic signals near the two points in time. Tables I and II show the rms values near $(8, 0)$ and $(8, 8)$, respectively, for the various computations. We note that the rms values for each fixed incompressible flow computation region exhibit convergent behavior.

Comparing the rms values for different flow regions, we do not see a clear convergent behavior; however, all values are within 5 per cent of the "exact" value. As the flow computation region changes, so does the acoustic source. Although the vorticity distribution is confined in a small region contained in the source region for all times, the source term used in our computations, however, does not have compact support. Our source is different from those favored by, for example, Powell [2] and Möhring [9], which depend explicitly on the vorticity distribution, and which thus have the same support as the vorticity distribution.

Figure 9 shows a typical contour plot of the acoustic source near the origin. Near the origin where the vorticity is concentrated, the forcing function has large

17

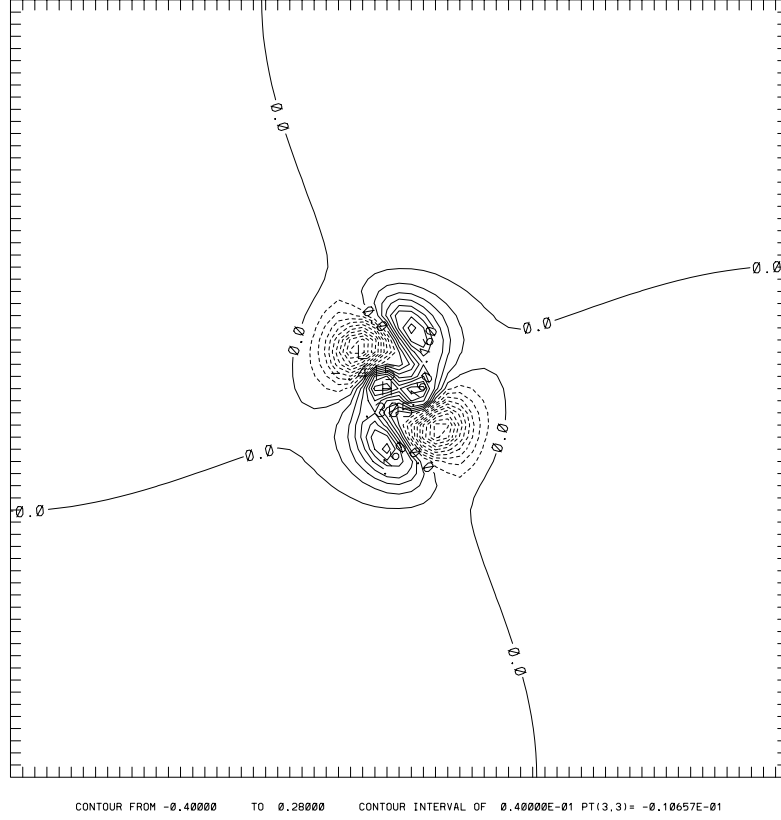CONTOUR FROM -0.40000   TO 0.28000   CONTOUR INTERVAL OF 0.40000E-01 PT(3,3)= -0.10657E-01

Figure 9: Contours of the acoustic source on $[-2, 2] \times [-2, 2]$ at $t = 2.0$.

magnitude and drops off rapidly. In all four flow regions used in this group of computations, the forcing functions are essentially the same here. Away from the center, however, the forcing function only decays as $1/r^2$.

We can understand the decay rate by considering the estimates below. The acoustic forcing function in Klainermann and Majda's formulation is

$$f = -\frac{1}{\gamma P_0}(p_t^\infty + v^\infty \cdot \nabla p^\infty),$$

the material derivative of the incompressible pressure. In a typical two-dimensional incompressible fluid flow with the vorticity confined in some bounded region, the magnitude of the velocity $|v^\infty|$ behaves as the inverse distance, that is,

$$|v^\infty| \sim \frac{1}{r} \text{ as } r \to \infty.$$
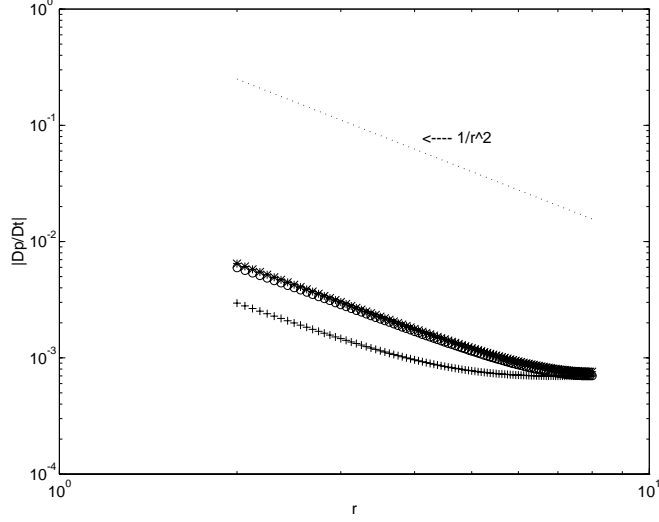
Figure 10: The acoustic source plotted as a function of the radial distance, along the radial lines $x = y$ ('+'), $x = 0$ ('*'), and $y = 0$ ('o'), for $r > 2$. The source is computed on $[-8, 8] \times [-8, 8]$, with $\triangle x = \triangle y = 1/16$.

This implies that

$$p^\infty \sim \frac{1}{r^2} \text{ as } r \to \infty.$$

Therefore we should have, at least,

$$f \sim \frac{1}{r^2} \text{ as } r \to \infty.$$

This behavior has been observed in our computations. Figure 10 shows a typical log-log plot of the acoustic source along radial lines $x = y$, $x = 0$, and $y = 0$, away from the origin. Indeed, we see that the source decays as $1/r^2$. We also see that the decay rate degrades near the boundaries of the flow region; we suspect that it is probably due to boundary conditions used in the computations of the incompressible pressure and the assumptions on the flow near the boundary. As the flow computation region is expanded, source errors due to limiting the domain and the boundary conditions should diminish.

Next we examine whether even larger incompressible flow computation regions have any significant effect on the acoustic signals. In the second group of experiments, we let the acoustics region be $[-16, 16] \times [-16, 16]$, with $\triangle x = \triangle y = 1/8$, and again we vary the size of the flow computation region, with a fixed spatial resolution of $\triangle x = \triangle y = 1/16$. The rms values of the acoustic

	$[-4,4]^2$	$[-6,6]^2$	$[-8,8]^2$	$[-12,12]^2$	$[-16,16]^2$
near $(8,0)$	4.410	4.473	4.644	4.654	4.625
near $(8,8)$	3.489	3.512	3.787	3.596	3.635

Table III: The rms values $\times 10^{-3}$ of the acoustic signals near $(8,0)$ and $(8,8)$, in the time intervals $[8,23]$ and $[10,25]$, respectively. The acoustics is computed on $[-16,16] \times [-16,16]$, with $\triangle x = \triangle y = 1/16$. The flow is computed on the regions $[-4,4] \times [-4,4]$, $[-6,6] \times [-6,6]$, $[-8,8] \times [-8,8]$, $[-12,12] \times [-12,12]$, and $[-16,16] \times [-16,16]$, with $\triangle x = \triangle y = 1/16$.

signals near $(8,0)$ and $(8,8)$ in the corresponding time intervals are presented in table III.

Table III shows that for both $(8,0)$ and $(8,8)$, the rms values of the acoustic signals computed using different flow regions are within about 10 per cent of each other. This indicates that features in the source term salient to sound production have been contained in smaller flow computation regions. We do not commit significant errors by assuming a compact support for our acoustic source.

When we compare rms values from this group of experiments to those in tables I and II, another problem emerges. While the rms values near $(8,0)$ are in fairly good agreement, the rms values near $(8,8)$ in table III are considerably smaller than those in table II. A quick glance at the plots of the acoustic signals in figure 11 confirms this observation. In this figure, we have plotted the acoustic signals computed on $[-16,16] \times [-16,16]$ and on $[-8,8] \times [-8,8]$, with the same flow computation and the same resolution on the acoustics region. At $(8,0)$, the two solutions are nearly identical, as expected, but at $(8,8)$, there are both amplitude and phase differences. The reason for the disparity in the rms values near $(8,8)$ is the outflow boundary conditions. We have not applied any special treatment at the corners where the outflow boundary conditions are the most problematic. The reflection, though having the same frequency, causes the phase and amplitude errors. Near $(8,0)$ the outflow boundary conditions generates minimal numerical reflection. These errors due to the boundary conditions should not be of great concern; future improvement of our algorithm shall include implementations of better outflow boundary conditions.

With these analyses in mind, we compute the flow on the region $[-4,4] \times [-4,4]$ and the acoustics on the region $[-8,8] \times [-8,8]$, for all subsequent runs in this subsection.

As an application to our numerical method, we study some physical aspects of the acoustic signals generated by the finite vortex sheet rollup. For a fixed blob radius, we examine the effect of the number of vortices in the discretization of the vortex sheet on the acoustic signal. We fix $\delta = 0.25$ and study the acoustic signal as a function of time near $(8,8)$ for $N = 100, 200$, and 400. In a vortex simulation, it is often difficult to tell, by observing the positions of the individual
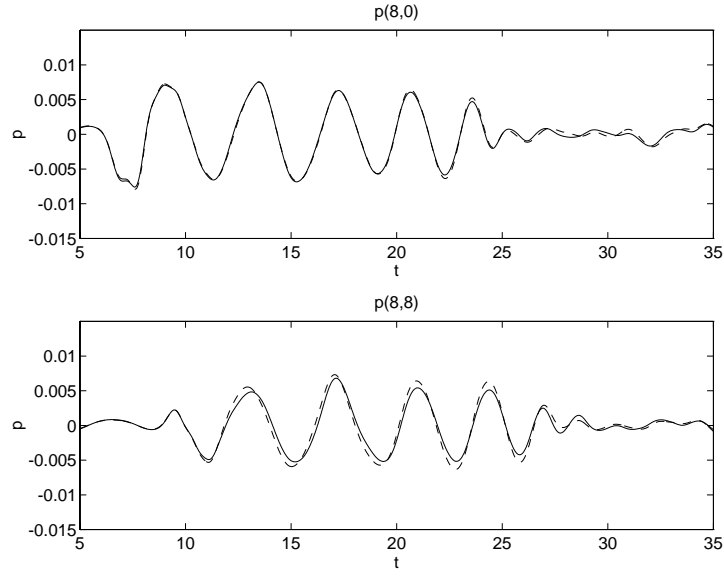
20

Figure 11: The acoustic pressure near $(8, 0)$ (top) and $(8, 8)$ (bottom) in time. The solid line represents acoustics computed on $[-16, 16] \times [-16, 16]$, while the dashed line represents acoustics computed on $[-8, 8] \times [-8, 8]$. Both have the same resolution of $\triangle x = \triangle y = 1/8$ on the acoustics region, and both are computed with the flow region $[-8, 8] \times [-8, 8]$ with a mesh of 256×256 panels.

blobs, whether enough vortex blobs have been used in a simulation. We have found that it is possible to use the acoustic signals due to a vortical configuration to determine the accuracy of the vortex motion simulation. For example, in this test problem, we see that using 100 blobs to represent the vortex sheet is not sufficient to simulate accurately the motion of the sheet, while using 200 vortex blobs seem to improve the resolution of the vortex motions, as the acoustic signal for $N = 200$ and $N = 400$ are very similar. This suggests that for the blob radius of 0.25, using 200 vortex blobs should be sufficient to resolve the motion of the vortex sheet.

For a fully resolved vortex sheet, the precession of two large composite vortices does not go on forever—the two vortices merge and form a single composite structure. For $N = 200$ and $N = 400$, the merger has occurred by about $t = 20$; we do not observe the merger for $N = 100$ because it occurs after the timespan of our computation. This merger in the vortex motion causes the acoustic signals to decrease. Figure 12 shows the acoustic pressure near $(8, 8)$ up to $t = 40$ for these three different N's. For $N = 200$ and $N = 400$, the pressure drops significantly around $t = 28$. There is a delay of about 8 time units from the approximate merger time. This drop in pressure can be understood by considering the effect of merger upon the acoustic source strength. Once the vortices have merged into a single structure, the core of this structure is more or less a radially symmetric distribution of vorticity, or a vortex patch. The vortices are moved by the inviscid Euler's equation in 2-D, which, in vorticity formulation, is

$$\frac{\partial \omega}{\partial t} + v \cdot \nabla \omega = 0, \tag{17}$$

The term $v \cdot \nabla \omega$ is very small, since the velocity of a vortex patch is in the tangential direction only, and the vorticity in the core is essentially radially symmetric. Equation (17) then implies that $\frac{\partial \omega}{\partial t}$ is also very small. Aerodynamic sound is due to the change of vorticity in time (see Möhring [9]). Thus, upon merging, the source of sound is diminished. This information has to be propagated to the point of observation, about 8 length units away from the source, at the sound speed of $c = 1$, and thus the delay time.

The sound before the merger of the two rolled-up ends is produced by the precession of the two concentrated blobs. Before the merger, the two blobs rotate about each other, approximately resembling the rigid rotation of two point vortices of equal strengths. In such rotations, the angular frequency is a constant. It is

$$\frac{\partial \theta}{\partial t} = \frac{\kappa}{4\pi a^2},$$

where κ is the vortex strength, and $2a$ is the distance between the vortices. The two vortices are indistinguishable, and so the configuration at any given time is identical to what it would be half a cycle later. Thus the fundamental acoustic
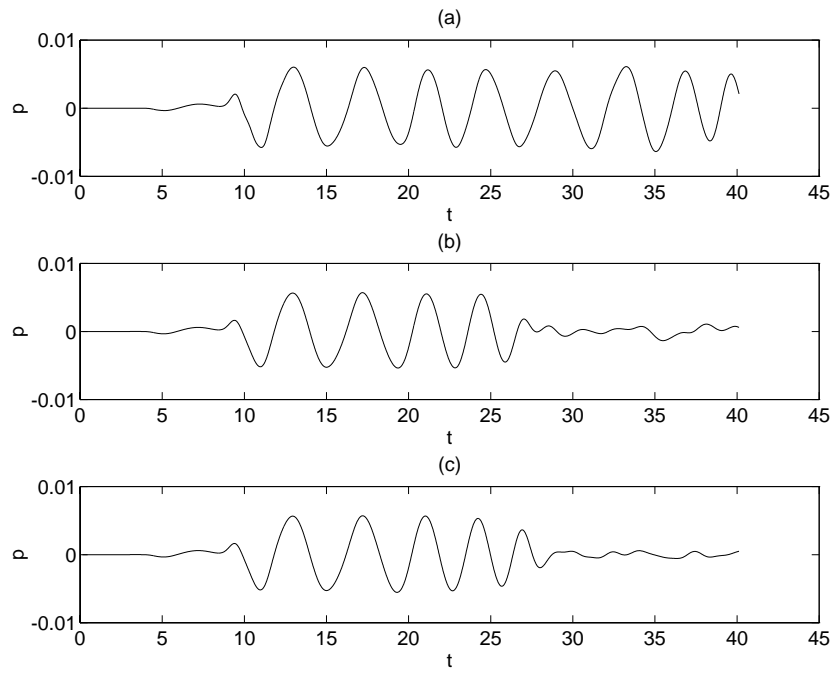
Figure 12: Acoustic pressure near $(8,8)$ as a function of time, computed using $\delta = 0.25$ and various numbers of vortices: (a) $N = 100$; (b) $N = 200$; (c) $N = 400$.

frequency should be twice the frequency of rotation, or

$$f_0 = \frac{1}{2\pi}\frac{\kappa}{4\pi a^2} = \frac{\kappa}{4\pi^2 a^2}.$$

In our vortex sheet, each of the two concentrated vortex blob contains exactly half of the total vorticity of 1.5. The distance between the centers of the two blobs is approximately 0.4, determined empirically by examining the positions of the vortices at various times. For $\kappa = 0.75$ and $a \approx 0.2$, we obtain $f_0 \approx 0.25$, in agreement with spectral analyses of the acoustic signals. As the two ends gradually merge, the distance between the two centers decreases, and the precession frequency increases. One may discern this slight frequency modulation of the acoustic signals in figure 12.

5.2   Sound Generation by a Wake Simulation

We compute the sound generated by a configuration of vortices simulating a finite vortex street. This simulation is due to Anderson [16]. In this simulation, two point vortices of equal and opposite strengths ± 0.85 are introduced at every time step at $(0, \pm 0.5)$, into a horizontal background flow of constant velocity $u = 1$. In addition, a single point vortex of strength $+1$ is injected into the fluid at $(0, 2)$ at the beginning of the simulation. The asymmetry causes the vortices to oscillate as they travel downstream, creating a flow pattern similar to that of a vortex street. The strength of a vortex is gradually decreased to zero after they have participated in the simulation for 10 time units, thus keeping the length of the vortex street finite. The time it takes for the vortex strength to decrease to zero is 5. Vortices of zero strength are removed, thus also keeping the number of vortices in the simulation finite. The vortices are moved according to the incompressible Euler's equations in Lagrangian form. The positions of the vortices in the course of the simulation at various times are shown in figure 13.

An indication of the frequency of oscillation in the vortex street is the vertical flow velocity at the origin. Figure 14 shows the vertical flow velocity at the origin in the course of the computation. After a "warm up" period of about 20 time units, the vertical velocity at the origin oscillates at a frequency of about 0.2. This is the characteristic frequency of the flow.

In the acoustics computation, the incompressible flow variables are extracted from the simulation on the region $[-8, 24] \times [-8, 8]$, with a grid of 128 by 64 panels. We solve the equations of acoustics on the region $[-16, 48] \times [-32, 32]$, with a grid of 256 by 256 panels. The flow is advanced with a time step of 0.1, while the acoustics is computed using a time step of 0.05. we let the vortices evolve up to $t = 50$ before starting the acoustics calculation. Homogeneous initial conditions are assumed for the acoustic variables. The approximate Mach number is 0.752 for these computations A spectral analysis of the vertical flow velocity in the course of the acoustics computation, starting at $t = 50$ is shown in figure 15.

24
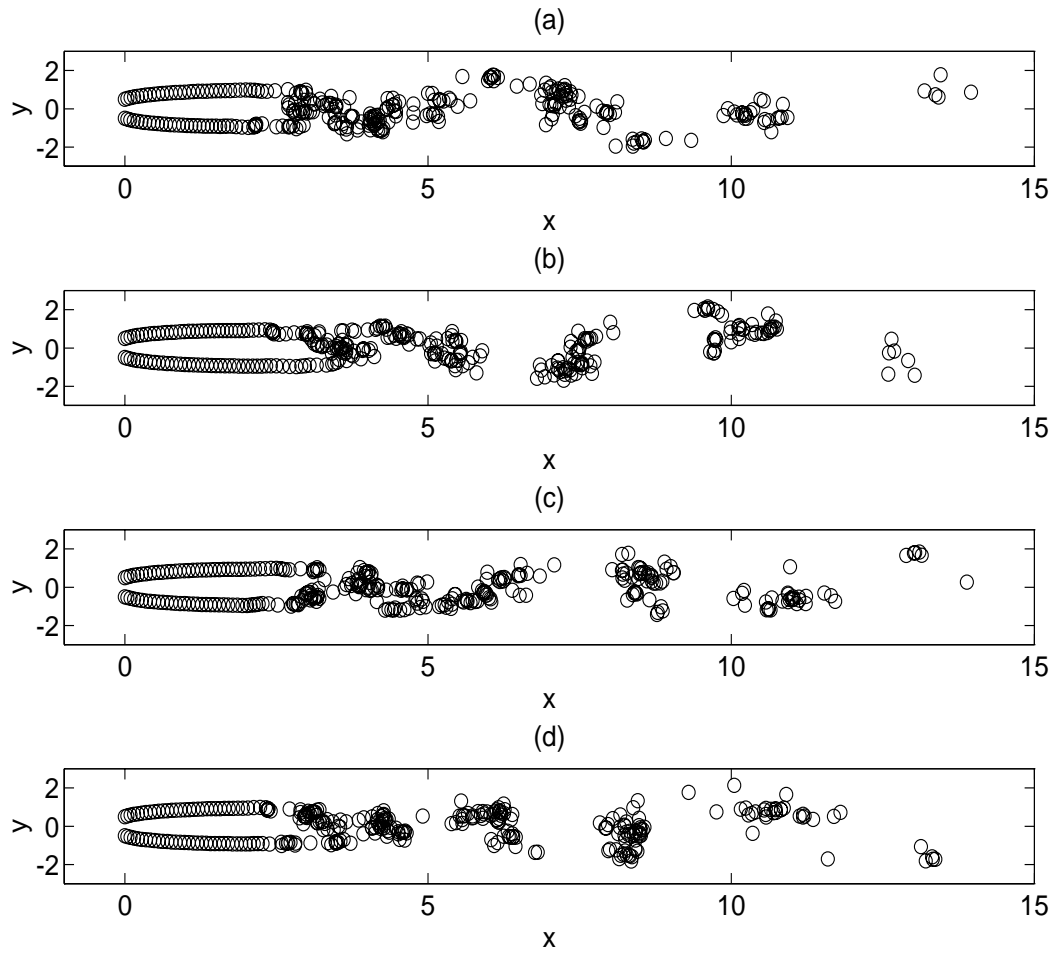
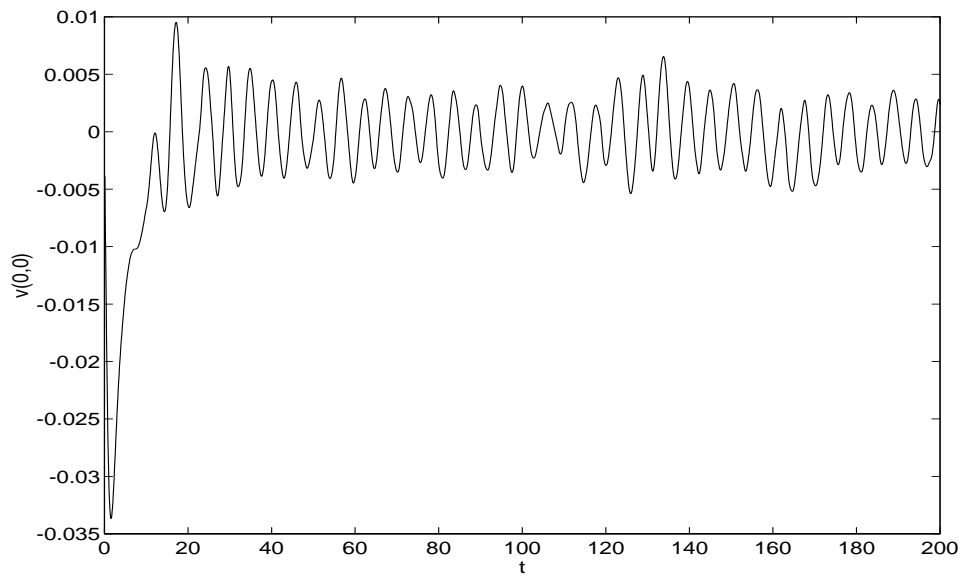Figure 13: The wake simulation at (a) $t = 25$ (b) $t = 50$ (c) $t = 75$ and (d) $t = 100$.

Figure 14: The horizontal flow velocity at the origin as a function of time. The frequency of oscillation is about 0.2.
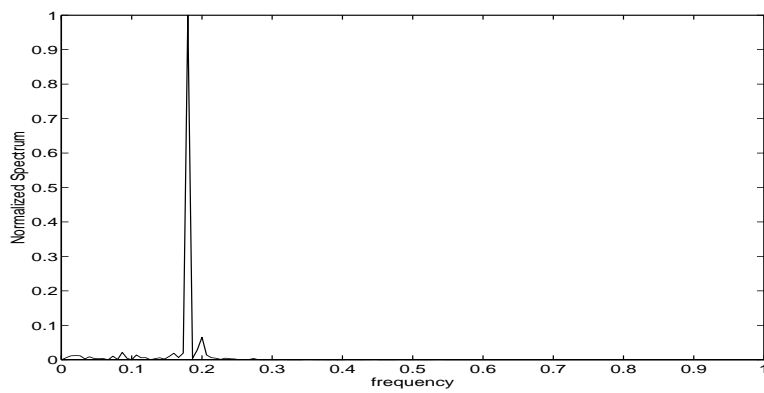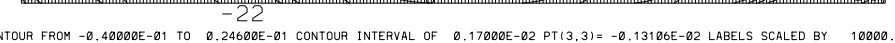

Figure 15: The spectrum of the horizontal flow velocity at the origin during the acoustics computation. The peak frequency is approximately 0.2.

26

CONTOUR FROM -0.40000E-01 TO 0.24600E-01 CONTOUR INTERVAL OF 0.17000E-02 PT(3,3)= -0.13106E-02 LABELS SCALED BY 10000.

Figure 16: Acoustic pressure contours in the region $[-16, 48] \times [-32, 32]$ at $t = 100$

In the acoustic field, waves are produced around the source region. These waves emanate outwards and are advected by the background flow. Complicated structures are seen in the source region. Doppler effect is observed; the waves are bunched up more tightly upstream than downstream. Figure 16 shows the acoustic pressure contours at $t = 100$. We examine the acoustic pressure as a function of time at various points. We collect data at points in the far field, points directly downstream along the x-axis, and points directly above the injection sites on the y-axis. Figure 17 shows the acoustic signal and its spectrum at a point near the right top corner of the computational domain, that is, a point in the far field. Figures $18 - 20$ show the acoustic signals and the normalized spectra at three points directly downstream, at $(32, 0)$, $(16, 0)$, and $(8, 0)$, respectively. And figures $21 - 23$ show the acoustic signals and the normalized spectra at three points directly above the injection sites, at $(0, 4)$, $(0, 8)$, and $(0, 16)$, respectively.

As shown in figure 17, the sound pressure in the far field peaks at the frequency of about 0.2, same as the characteristic frequency of the flow. At points directly downstream but outside the wake, as seen in figures 18 and 19, the sound pressure has a peak frequency of about 0.4, or twice the fundamental frequency. At points directly downstream but inside the wake, as seen in figure 20, the acoustic signals are comprised of waves of various frequencies, with the strongest component having the frequency of 0.4. At points above the injection sites the sound, as seen in figures 21 and 22, pressure has a peak frequency of about 0.2. As one gets further away from the injection sites, a component at the frequency of 0.1 becomes stronger, as shown in figure 23, No other harmonics of the fundamental frequency is significantly present.

We compare these results with numerical results obtained by Hardin and Lamkin for the flow past a circular cylinder [17], although ours come from an inviscid computation, no cylinder is present in our flow, and our simulation is finite within the computational domain of the acoustics and by no means physical. Hardin and Lamkin have found that in the sound signals, even harmonics of the fundamental frequency of a flow past a cylinder, or the Strouhal frequency, are present directly downstream, while odd harmonics of the Strouhal frequency are present above the cylinder. Their findings agree with available measurements (see [18] and [19]). Our results basically agree with those of Hardin and Lamkin's. The differences may be attributed to properties of the wake simulation and the acoustics computation: in the far field, the finite vortex street is seen only as a source oscillating at the characteristic frequency, thus we only get the fundamental frequency there; while well within the finite wake, there may be features of the wake simulation that cause the spectrum to broaden; the extraneous peak at 0.1 is probably due to initialization of acoustics computation; both the initial conditions of the acoustics equations and the starting time of the acoustics computation affect the relative magnitude of this component, and it is only a transient effect.
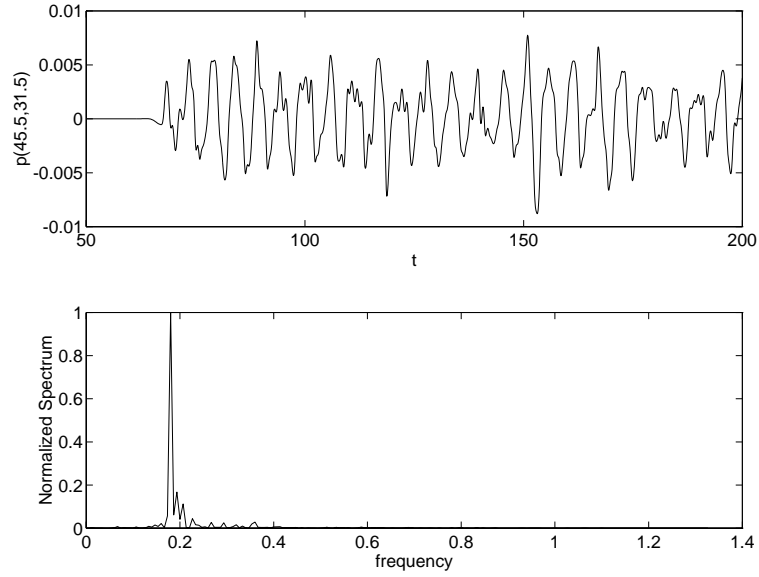
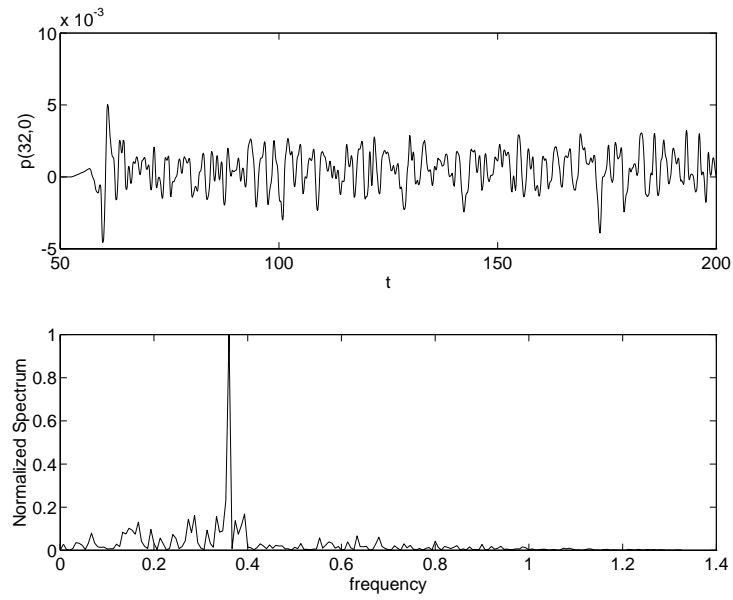Figure 17: Acoustic signal near $(46, 32)$ and its normalized spectrum.

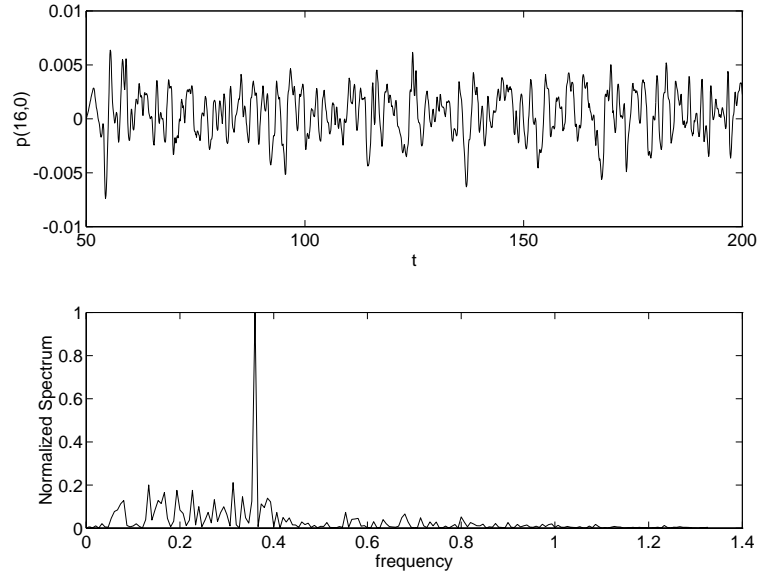Figure 18: Acoustic signal near $(32, 0)$ and its normalized spectrum.

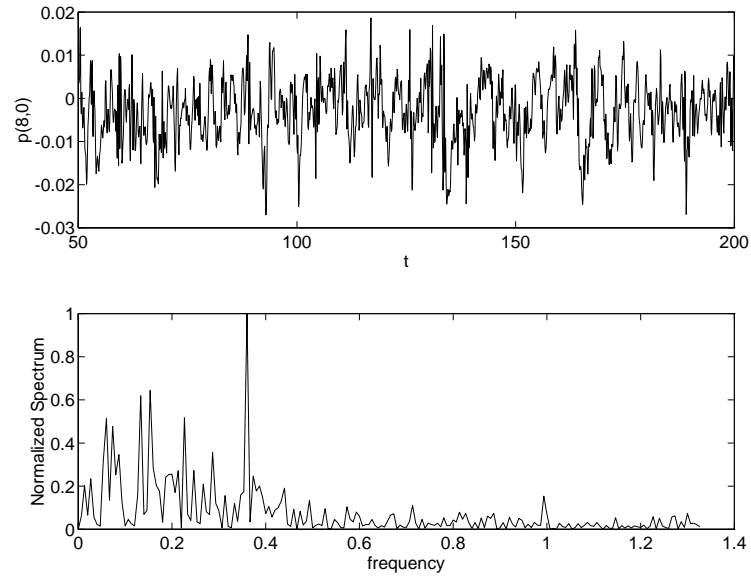Figure 19: Acoustic signal near $(16, 0)$ and its normalized spectrum.

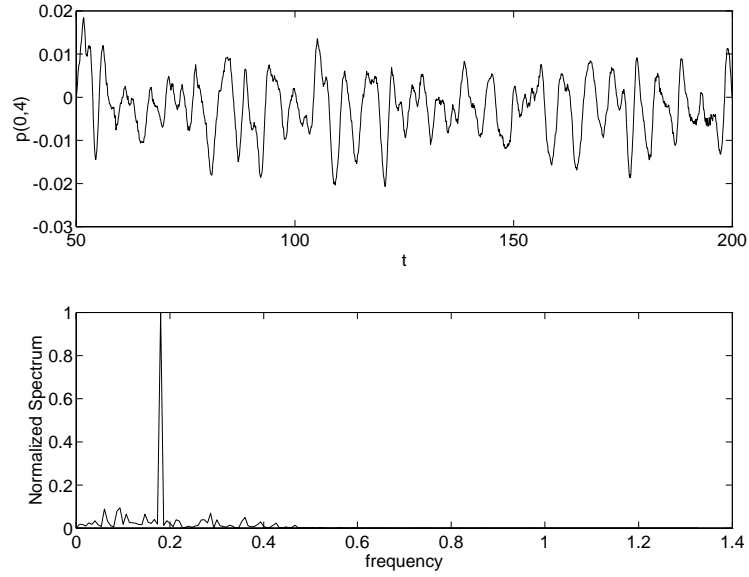Figure 20: Acoustic signal near $(8, 0)$ and its normalized spectrum.

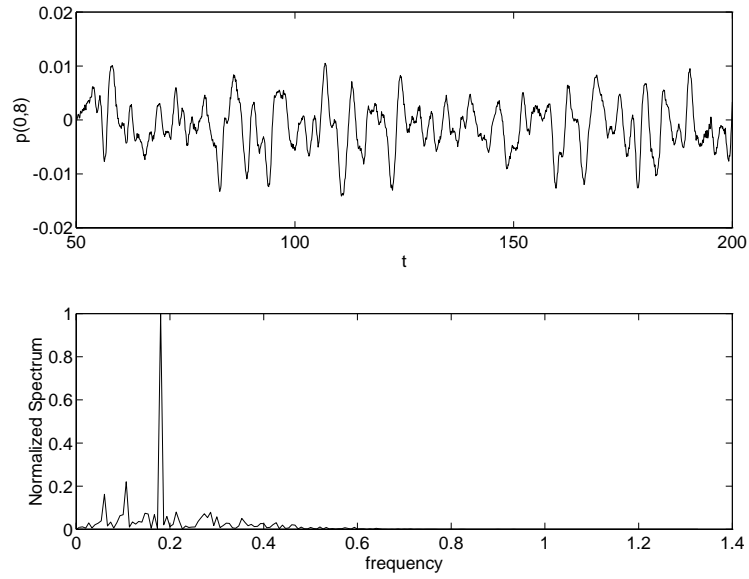Figure 21: Acoustic signal near $(0, 4)$ and its normalized spectrum.

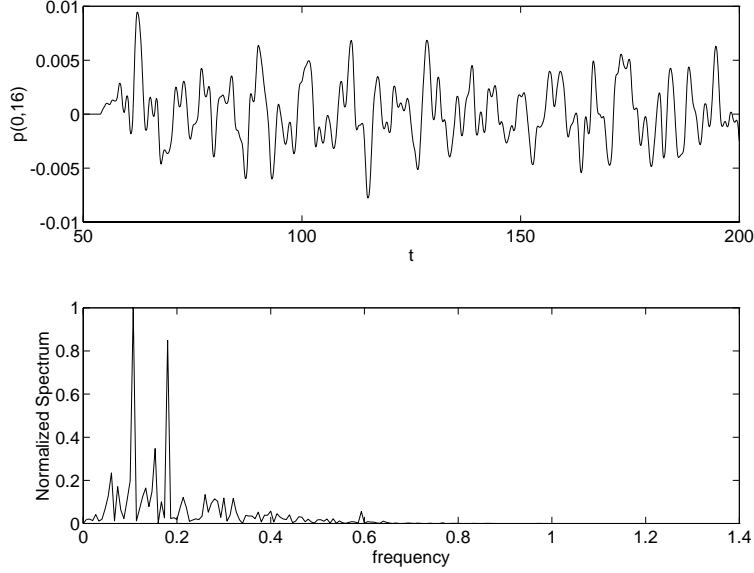Figure 22: Acoustic signal near $(0, 8)$ and its normalized spectrum.

Figure 23: Acoustic signal near $(0, 16)$ and its normalized spectrum.

6   Conclusions and Future Work

This investigation was begun in an effort to assess the feasibility of computing the acoustic signals in low Mach number flows by computing corrections to the incompressible flows. Our computational results show that this approach may be a useful alternative to direct numerical solutions of slightly compressible problems.

Many improvements of the current algorithm can be made. In order to make our algorithm more useful for flows with smaller Mach numbers, we need to improve the representation of the fine source on the coarse grid. More sophisticated grid composition techniques can be incorporated into our method. Methods such as composite grid (CMPGRD) [20] or adaptive mesh refinement (AMR) (see, for example, [21]) may be used in the acoustics calculations, the incompressible computations, or both.

Our numerical technique may be used as a diagnostic tool for various incompressible flow phenomena. We have already seen how it may help us to determine whether a numerical discretization is sufficient. Furthermore, our technique may allow us to "listen in" on the formation of the singularities, and the acoustic signals may be used to classify them, as done analytically by Caflisch and Lund [22].

Our technique may easily be modified to compute sound generation in 3-D flows with no boundary, since the asymptotic expansions are valid for any num-

32

ber of space dimensions. The usefulness of our technique will be closely linked to the availability of three dimensional incompressible data. Supercomputing techniques will be necessary in three-dimensional computations. We would also like to extend our technique to investigate the sound generation process by flows with boundaries, such as flow past an object, and flows involving chemical or thermal processes, such as low Mach number combustion; for these problems, further studies of the asymptotics are needed.

References

[1] Lighthill, M.J., *Proc. Roy. Soc.*,**A 211**, 564-587 (1952).

[2] Powell, A., *J. Acous. Soc. Am.*, **36**, 177-195 (1964).

[3] Curle, M.J., *Proc. Roy. Soc.*,**A 231**, 505-514 (1955).

[4] Crow, M.S., *Stud. Appl. Math.*, **49**, vol. 1, 21-44 (1970).

[5] Howe, M.S., *J. Fluid Mech.*, **67**, 596-610 (1975).

[6] Kambe, T., *J. Fluid Mech.*, **173**, 643-666 (1986).

[7] Mueller, E., Obermeier, F., *Proceedings of the IUTAM Symposium on Fundamental Aspects of Vortex Motion*, 43-51 (1988).

[8] Crighton, D. G., *Goals for Computational Aeroacoustics*, 3-20, *Computational Acoustics: Algorithms and Applications*, D. Lee, R. L. Sternberg, M.H. Schultz, ed., Elsevier Science Publishers, 1988.

[9] Möhring, W., *J. Fluid Mech.*, **85**, 685-691 (1978).

[10] Klainermann, S., Majda, A., *Comm. Pure Appl. Math.*, **35**, 629-651 (1982).

[11] Majda, A., *Compressible Fluid Flow and Systems of Conservation Laws*, Springer-Verlag, 1981.

[12] Pao, K., *Computational Aeroacoutics of Low Speed Flows in Two Dimensions*, Ph.D. dissertation, Department of Mathematics, University of California, Los Angeles (1993).

[13] Engquist,B., Majda, A., *Math. Comp.*, **31**, 629-651 (1977).

[14] Colella, P., *J. Comp. Phys.*, **87**, 171-200 (1990).

[15] Anderson, C. R., Greengard, C., SIAM J. Numer. Anal., **22**, 413-440 (1985).

[16] Anderson, C. R., *A Finite Vortex Street Model*, UCLA CAM Report 93-01 (1993).

[17] Hardin, J. C., and Lamkin, S. L., *AIAA Journal*, **22**, vol. 1, 51-57 (1984).

[18] Etkin, B., Korbacher, G. K., and Keefe, R. T., *J. Acous. Soc. Am.*, **29**, vol. 1, 3–36 (1957).

[19] Gerrard, J., H., *Proc. Phys. Soc. (London)* B, **68**, 453-461 (1955).

[20] Brown, D. L., Chesshire, G., Henshaw, B., *Getting Started with CMPGRD: Introductory User's Guide and Reference Manual*, Los Alamos National Laboratory Technical Report LA-UR-90-3729 (1990).

[21] Berger, M. J., and Oliger, J., *J. Comp. Phys.*, **53**, 484 (1984).

[22] Caflisch, R. E., and Lund, F., *Phys. Fluids* A, **1** (6), 909-910 (1989).

List of Figures